UC Santa Cruz
UC Santa Cruz Previously Published Works

Title

Regulated Interfacial Proton and Water Activity Enhances Mn2+/MnO2 Platform Voltage and Energy Efficiency

Permalink

Journal

ISSN

Authors

Xue, Xinzhe

Liu, Zhen

Eisenberg, Samuel

et al.

Publication Date

DOI

Copyright Information

Peer reviewed

Regulated Interfacial Proton and Water Activity Enhances Mn^{2+}/MnO_2 Platform Voltage and Energy Efficiency

Xinzhe Xue, Zhen Liu, Samuel Eisenberg, Qiu Ren, Dun Lin, Emma Coester, Heng Zhang, Jin Z. Zhang, Xiao Wang,* Yat Li*

Department of Chemistry and Biochemistry, University of California, 1156 High Street, Santa Cruz, California, 95064 United States of America

* Corresponding authors: xwang431@ucsc.edu and yatli@ucsc.edu

Abstract

Electrolytic MnO_2 batteries store charges via the Mn^{2+}/MnO_2 two-electron transfer process with higher capacity and voltage than conventional one-electron (Zn^{2+} or H^+) intercalation reactions. Yet, the opposite effect of interfacial H^+ on the dissolution/deposition processes and the role of interfacial H_2O are rarely discussed. Here we introduce tetrafluoroborate anion (BF_4^-) into the sulfate-based electrolyte to regulate the interfacial H^+ and H_2O activity. First, BF_4^- hydrolysis increases the electrolyte's acidity, promoting MnO_2 dissolution. Second, BF_4^- forms an H-bond network with interfacial H_2O that assists H^+ diffusion while retaining sufficient H_2O supply to facilitate MnO_2 deposition. As a result, the cathode-free $Zn//MnO_2$ electrolytic cell achieves a high plateau of ~1.92 V and energy efficiency of ~84.23 % in the BF_4^- containing electrolyte. Significantly, the cell delivers 1000 cycles at 1 C with ~100 % Coulombic efficiency and a high energy efficiency retention of 93.65 %. Our findings disclose a new strategy to promote Mn^{2+}/MnO_2 platform voltage and energy efficiency.

Aqueous zinc battery (AZB) is one of the most promising energy storage systems for large-scale applications due to its high safety, low cost, and environmental friendliness.[1-3] To match the high capacity of zinc metal (~820 mAh g^{-1}), various cathode materials, such as oxides,[4, 5] open structure analogues,[6] chalcogens,[7-9] and halogens,[10, 11] have been explored for AZBs. Among them, manganese dioxide (MnO$_2$) has been considered to be one of the most attractive candidates due to its high capacity (~308 mAh g^{-1} for one-electron transfer) and adequate redox potential (~0.70 V vs. SHE).[12] Recently, the MnO$_2$ dissolution/deposition charge storage mechanism has been demonstrated to further increase the voltage and capacity of Mn-based AZBs.[13] The dissolution/deposition (Mn^{2+}/MnO$_2$) is a two-electron transfer process, which doubles the theoretical capacity of MnO$_2$ cathode to ~616 mAh g^{-1} and considerably increases the redox potential (~1.229 V vs. SHE).[14-16] The charge storage via the dissolution/deposition mechanism pushes the aqueous-based energy density even higher, to over 1000 Wh kg^{-1}.[17]

However, this charge storage mechanism involves liquid-solid transition, and the thermodynamics and kinetics of this reaction are highly dependent on the acidity and interfacial environment.[18-20] On one hand, protons have been found to play an important role in MnO$_2$ dissolution.[18] According to the dissolution Nernst Equation:

$$E = E^{\Theta} + \frac{RT}{nF} \ln \left(\frac{[H^+]^4}{[Mn^{2+}]} \right) \tag{1}$$

where E^{Θ} is the standard potential, R is the gas constant, T is temperature, n is the number of electrons transferred during redox reactions, F is the Faraday's constant, [H$^+$] and [Mn^{2+}] are the concentrations of proton and Mn^{2+}, [H$^+$] exponentially affects the dissolution potential, E. A higher [H$^+$] favors MnO$_2$ dissolution (Equation 2) and therefore increases the high voltage Mn^{2+}/MnO$_2$ capacity.

$$MnO_2 + 4H^+ + 2e^- \leftrightarrow Mn^{2+} + 2H_2O \tag{2}$$
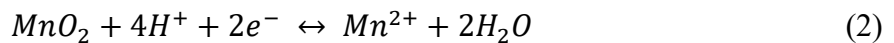
On the other hand, the generation of interfacial protons has the opposite effect on the MnO$_2$ deposition on electrodes (the reverse process in Equation 2), in which protons are produced during the process. The generation and accumulation of protons on the electrode surface will increase the interfacial acidity, which inevitably disturbs MnO$_2$ deposition and causes nonuniform deposition, MnO$_2$ detachment, and thus, battery degradation.[21] Also, high interfacial [H$^+$] will rapidly increase the deposition overpotential, as shown in the deposition Nernst equation (Equation 3).

$$E' = E^{\Theta} - \frac{RT}{nF} \ln \left(\frac{[Mn^{2+}]}{[H^+]^4} \right) \tag{3}$$

A higher deposition voltage E' will lead to a lower energy efficiency, and even cause the early termination of the process.[19] Therefore, a proton-rich interfacial environment can negatively affect the system's efficiency and stability during the deposition process.

Previous studies showed that the Mn^{2+}/MnO$_2$ conversion efficiency can be tuned by adjusting the properties of the electric double layer (EDL) formed at the interface between the electrode and electrolyte. For example, Liang and co-workers introduced carboxylate anions into the electrolyte system.[19] The small ionization constant of carboxylic acid enhances the capability of dragging protons out of EDL, which is favorable for MnO$_2$ deposition. However, the strong bonding between protons and carboxylate anions reduces the MnO$_2$ dissolution potential by ~0.50 V. Enhancing interfacial proton diffusion without sacrificing operating voltage is challenging. Moreover, unlike metal anodes, the Mn^{2+}/MnO$_2$ reaction also involves water molecules. In addition to proton diffusion, interfacial water activity also plays a critical role in determining deposition efficiency and dissolution voltage, which has not been considered in previous studies yet.

Here we demonstrate a new strategy to simultaneously achieve high platform voltage and Mn^{2+}/MnO$_2$ energy efficiency via controlled regulation of interfacial proton and water activity.

Our strategy is introducing tetrafluoroborate anion (BF_4^-) into the commonly used sulfate (SO_4^{2-}) electrolyte system to regulate interfacial properties. **Figure 1** illustrates the electrode-electrolyte interfacial environment with or without BF_4^- regulation in a sulfate-based electrolyte ($ZnSO_4$ and $MnSO_4$). We anticipated that BF_4^- has two functions. First, BF_4^- can lower the electrolyte pH via hydrolysis in aqueous media. A proton rich environment facilitates high voltage MnO_2 dissolution (higher discharge voltage). Second, the fluoride-rich anion can modulate water activity by forming hydrogen bond (H-bond) network at the interface to provide proton with fast diffusion pathways while maintaining sufficient water supply. The balanced interfacial activities favor efficient and uniform MnO_2 deposition. Taken together, the BF_4^- regulated interface could increase the platform voltage and energy efficiency of $Zn//MnO_2$ electrolytic cell.
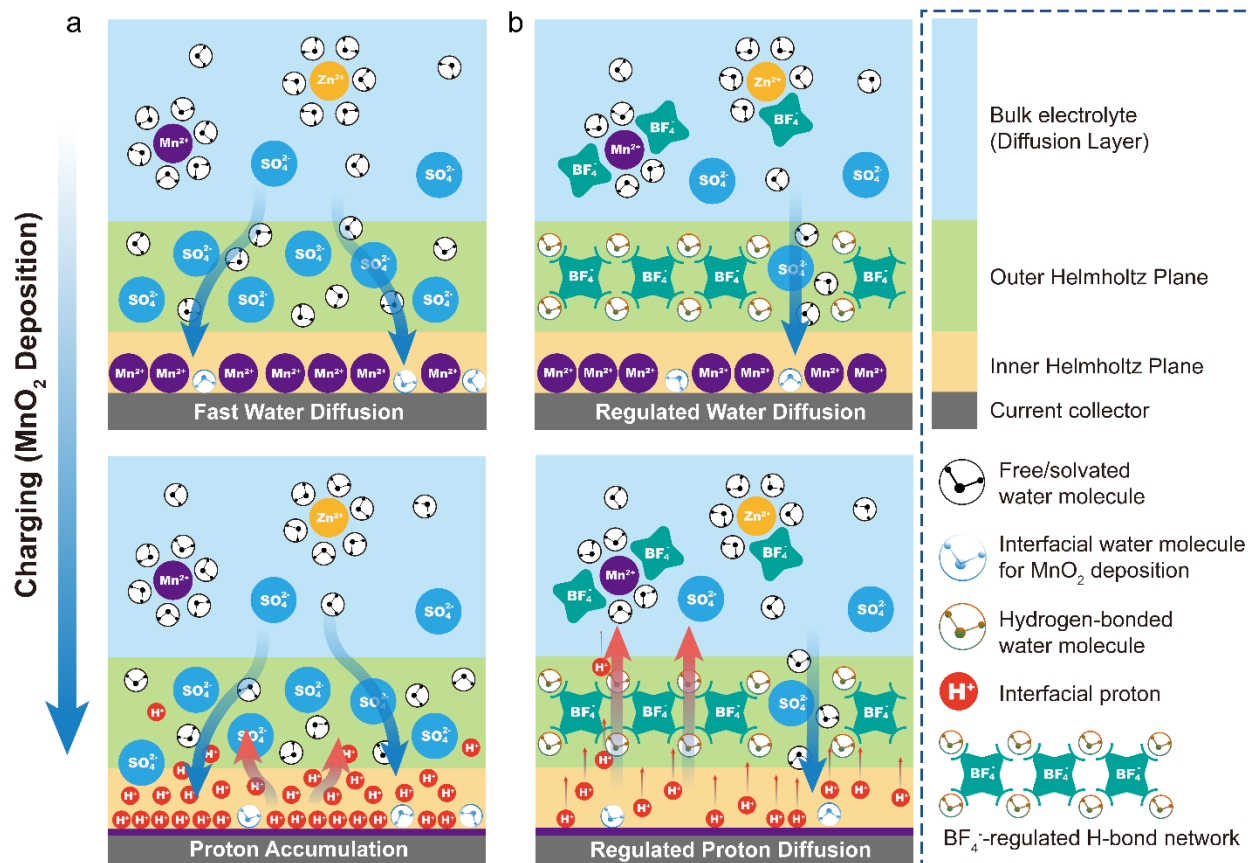
Figure 1. Schematic illustration of the interfacial environments with/without BF_4^- regulation during the deposition process: (a) in the absence of BF_4^-, the slow proton diffusion causes proton accumulation; (b) in the presence of BF_4^-, the H-bond network regulates and balances proton diffusion and water supply.

To test our hypothesis, we first investigated the effect of BF_4^- on increasing electrolyte's acidity. A previous study reported that BF_4^- anion will reach an equilibrium of 4 % intrinsic hydrolysis in aqueous media (Equation 4):[22, 23]

$$BF_4^- + H_2O \leftrightarrow BF_3OH^- + HF \tag{4}$$
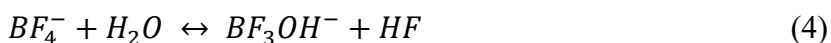
As a result, the addition of BF_4^- can increase the proton concentration in the electrolyte without the need to add acid. **Figure S1** (Supporting Information) shows the pH values of sulfate-based

6

electrolytes containing different concentrations of $Zn(BF_4)_2$. The initial pH of 2.0 M $ZnSO_4$ + 0.50

M $MnSO_4$ electrolyte is 3.2 (denoted as SO_4-3.2). It decreases to 1.5 after substituting $ZnSO_4$ with

2.0 M $Zn(BF_4)_2$ (denoted as BF_4-SO_4-1.5). The hydrolysis of the BF_4^- was confirmed by the ^{19}F

NMR spectrum of BF_4-SO_4-1.5 electrolyte (**Figure S2**, Supporting Information), which contains

two peaks that can be attributed to BF_4^- and hydrolyzed BF_3OH^-. With the increased acidity, MnO_2

electrochemical dissolution is expected to take place at a higher voltage and efficiency. **Figure 2a**

shows the galvanostatic discharge curves of a cathode-free $Zn//MnO_2$ device obtained at 1.0 mA

cm^{-2} in different electrolytes. In BF_4-SO_4-1.5 electrolyte, the device has the most obvious and

continuous discharge platform above 1.8 V, which is contributed by the two-electron transfer of

Mn^{2+}/MnO_2 dissolution process. Compared with the sulfate electrolyte with the same initial pH

(SO_4-1.5), the BF_4-SO_4-1.5 electrolyte delivers a higher and continuously increasing energy

efficiency within 90 cycles (**Figure 2b** and **Figure S3**, Supporting Information). This is likely

because of the hydrolytic equilibrium of BF_4^- providing sufficient proton supply, as evidenced in

the change of pH profile obtained at fully discharged states (**Figure S4**, Supporting Information).

The continuously extended high discharge platform observed in BF_4-SO_4-1.5 electrolyte yields

both higher Mn^{2+}/MnO_2 two-electron capacity contribution (~73.59%) and overall energy
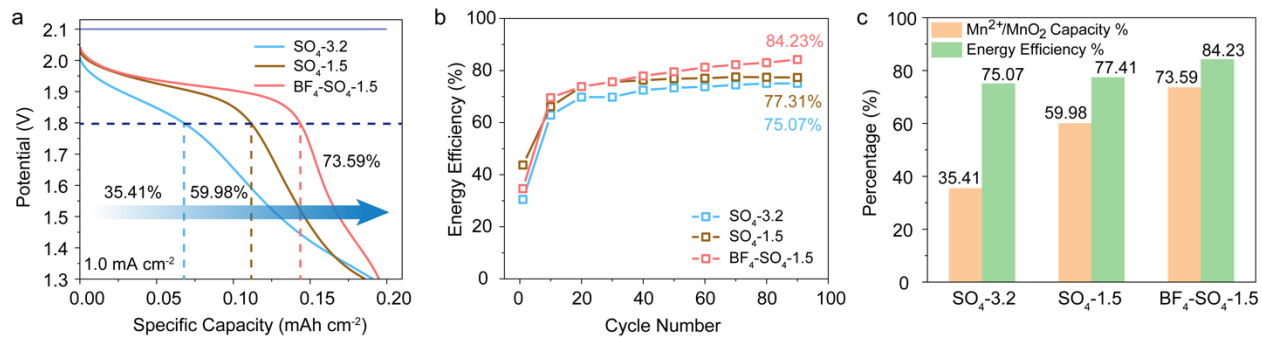
efficiency of 84.23% (**Figure 2c**).

Figure 2. (a) The galvanostatic discharge curves of a Zn//MnO$_2$ device collected at 1.0 mA cm^{-2} in different electrolytes. The values represent the Mn^{2+}/MnO$_2$ capacity contribution percentage above 1.8 V. (b) The changes in the device's energy efficiency within the first 90 cycles in different electrolytes. (c) The percentage of Mn^{2+}/MnO$_2$ capacity contribution and energy efficiency obtained in different electrolytes.

In addition to regulating electrolyte pH, BF$_4^-$ interacts with H$_2$O molecules via H-bonds for regulating interfacial environment as well as modulates cation solvation structures to boost the MnO$_2$ deposition/dissolution and cation de-solvation kinetics. Fluorine as a H-bond acceptor was reported to have the capability to regulate water activity via the formation of OH···F H-bonds.[24, 25] The Fourier-transform infrared spectroscopy (FTIR) spectra collected from the two sulfate-only electrolytes confirmed the presence of the S-O bonds, which located at ~1075 cm^{-1} (**Figure 3a**). In BF$_4$-SO$_4$-1.5 electrolyte, this peak shifts to ~1050 cm^{-1} and becomes broader. It can be further deconvoluted into two peaks (**Figure S5**, Supporting Information) corresponding to the stretching vibration of the B-F and S-O bonds. Besides, the peak located at ~3600 cm^{-1} verifies that OH···F H-bonds formed between BF$_4$ and H$_2$O molecules (**Figure 3b**), which wasn't observed in sulfate-only electrolytes.

The formation of BF$_4$-H$_2$O H-bonds regulates the interfacial environment to promote deposition/dissolution efficiency. Due to the high symmetry and highly electronegative fluorine atoms, it has been reported that BF$_4^-$ is capable of forming multi-H-bonds with H$_2$O molecules and regulating a 3D H-bond network for Grotthuss proton transfer.[26, 27] Here we calculate the adsorption energies of BF$_4^-$ and SO$_4^{2-}$ on the ε-MnO$_2$ surface using periodic DFT to provide insights into the anion adsorption process during the formation of the BF$_4$-H$_2$O H-bond network.

The XRD analysis of the MnO_2 electrode shows that the deposited MnO_2 is ε-MnO_2 (**Figure S6**, Supporting Information). After testing for 1000 cycles in the Zn-MnO_2 device, the MnO_2 electrode exhibits the same set of diffraction peaks but the (101) peak is substantially enhanced while the (102) peak has almost disappeared. The results suggest the (101) facet is dominant in regulating the electrolyte/electrode interface. **Figure 3c** shows the adsorption structure of BF_4^- and SO_4^{2-} on the ε-MnO_2 (101) surface. The calculated adsorption energy of BF_4^- is 2.67 eV, which is notably higher than that of SO_4^{2-} (0.99 eV), suggesting that BF_4^- is preferable at the electrode/electrolyte interface to form the BF_4-H_2O network in the hybrid electrolyte (**Table S1**, supporting information).

In addition, many studies have shown that regulated cationic solvation structures can improve the kinetics of the solvation/de-solvation process.[28] Typically, Zn^{2+} and Mn^{2+} in aqueous systems are stably coordinated with up to six water molecules as Zn^{2+}-$(H_2O)_6$ and Mn^{2+}-$(H_2O)_6$.[28, 29] In the presence of BF_4^-, metal cations can also coordinate to BF_4^- rather than H_2O.[24] Here, we investigated the cationic solvation structures in BF_4-SO_4-1.5 electrolyte system using a combination of density functional theory (DFT) simulations and Raman spectroscopy. In DFT simulations, we present the solvation structure of Mn^{2+} with only its first solvation shell that contains six molecules, i.e. Mn^{2+}-$(BF_4)_x(H_2O)_{6-x}$ (x = 0-6). The initial solvation structures are obtained by replacing water molecules in an octahedral Mn^{2+}-$(H_2O)_6$ with BF_4^- anions; the fully optimized structures with various BF_4^- coordination numbers are shown in **Figure 3d**. Among these structures Mn^{2+}-$(BF_4)_2(H_2O)_4$ gives the most negative formation energy (**Table S2**, supporting information), indicating its highest thermodynamic stability. The Raman spectra of SO_4-3.2 and SO_4-1.5 electrolytes (**Figure 3e**) show only one peak centered at ~390 cm^{-1}, corresponding to the solvated structure Zn^{2+}-$(H_2O)_6$. In contrast, BF_4-SO_4-1.5 electrolyte exhibits

a broad peak between 300 and 425 cm^{-1}, which can be deconvoluted into two peaks indicating the presence of two solvated Zn^{2+} structures, Zn^{2+}-$(BF_4)_x(H_2O)_{6-x}$ and Zn^{2+}-$(H_2O)_6$.

To further verify the effect of introducing BF_4^- into the electrolyte on the MnO_2 deposition kinetics, the constant current deposition at 1.0 mA cm^{-2} was conducted in the hybrid (BF_4-SO_4-1.5) and pure sulfate (SO_4-1.5) electrolyte systems under the same pH condition (**Figure 3f**). Before reaching the voltage for MnO_2 deposition, it was observed that there is a voltage rising area (Z_1) in both electrolytes, which corresponds to the one-electron transfer process, H^+ and Zn^{2+} desertion (Mn^{3+}/Mn^{4+}), in the accumulated MnO_2 on the substrate.[15] The hybrid electrolyte has a lower one-electron capacity contribution, due to the higher dissolution/deposition efficiency (less MnO_2 accumulated on the substrate). We believe the enhancement can be attributed to the faster interfacial proton diffusion via the Grotthuss proton transfer mechanism because of the presence of BF_4-H_2O H-bond network in the hybrid electrolyte. Significantly, unlike the continuously increasing deposition voltage required in the pure sulfate system, the hybrid system shows not only lower but also more stable deposition voltage than the pure sulfate system (~40 mV), indicating the improved kinetics of cationic de-solvation process.
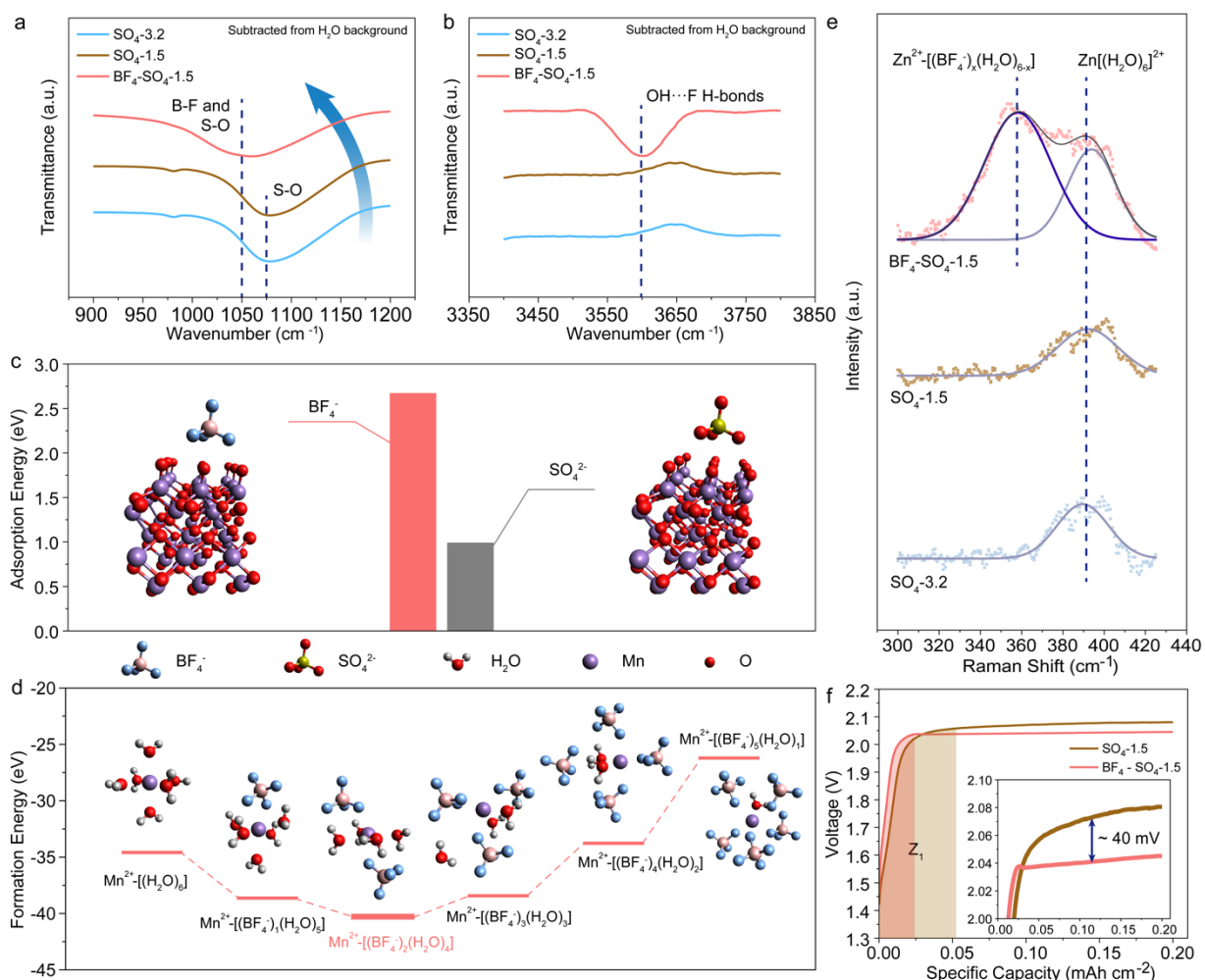
Figure 3. (a, b) FTIR spectra of different electrolytes. The dashed lines highlight B-F bond and OH···F H-bond. (c) DFT optimized adsorption structures of BF_4^- (left) and SO_4^{2-} (right) on ε-MnO_2 (101) surface and their corresponding adsorption energies. (d) DFT simulated solvation structures of Mn^{2+} and their corresponding formation energies. (e) Raman spectra of different electrolytes. The dots are experimental data. The solid black lines are fitted curves. The purple and gray curves are deconvoluted peaks. Dashed lines highlight the peak positions. (f) MnO_2 deposition voltage at $1.0\,mA\,cm^{-2}$ in BF_4-SO_4-1.5 and SO_4-1.5 electrolytes. Inset: magnified region to show the deposition voltage difference in the two electrolytes.

While the hybrid electrolyte promotes Mn^{2+} de-solvation and proton transfer via the BF_4-H_2O H-bond network, the excess BF_4 anions could also restrict the availability of interfacial water molecules and negatively affect the Mn^{2+}/MnO_2 conversion efficiency. $Zn//MnO_2$ devices assembled with Zn anode and bare carbon cloth cathode were tested in two different electrolytes, the BF_4^- electrolyte consisting of 2.0 M $Zn(BF_4)_2$ + 0.50 M $Mn(BF_4)_2$ (denoted as BF4-0.9) and the 2.0 M $ZnSO_4$ + 0.50 M $MnSO_4$ electrolyte with the same pH (denoted SO4-0.9), under the same conditions. **Figures 4a and b** show the 1st and 10th galvanostatic discharge curves obtained at 1.0 mA cm^{-2} in the two electrolyte systems. The initial Coulombic efficiency (CE) obtained in the SO4-0.9 electrolyte is ~62.5%, while it is almost 0% in the BF4-0.9 electrolyte (**Figure 4a**). It reflects that the MnO_2 deposition is substantially more efficient in SO4-0.9 electrolyte. At the 10th cycle (**Figure 4b**), the device in BF4-0.9 electrolyte exhibits a platform voltage of ~1.9 V, which is ~500 mV lower than that in SO4-0.9, and a lower CE of only 62.5%. Since the two electrolytes have the same acidity, the observed lower voltage platform and CE in BF4-0.9 is believed to be due to the insufficient supply of water molecules at the BF_4^- fully regulated interface (**Figure S7**, Supporting Information). **Figure 4c** shows the charging time and average charging current density at the initial cycle for 0.20 mAh cm^{-2} cells in different electrolyte systems to compare the deposition efficiencies. In general, under a higher acidity condition, the charging (deposition) time is expected to be longer. BF4-SO4-1.5 electrolyte has the highest deposition efficiency (shortest deposition time) among the low pH electrolyte systems and even comparable with SO4-3.2. In contrast, BF4-0.9 has an ultra-long charging time of ~1.5 hours and the extremely low average charging current density of only ~0.05 mA cm^{-2} even though it has a more preferable pH.

Besides, we also compared the MnO_2 deposition voltage in different electrolytes at a constant current density of 1.0 mA cm^{-2}. As shown in **Figure 4d** and **S8** (Supporting Information),

the device achieves the lowest deposition voltage in the BF_4-SO_4-1.5 electrolyte compared to other electrolytes with the same or even lower pH, suggesting that MnO_2 deposition is highly favorable. Notably, the BF_4-0.9 system has the highest deposition of 2.2 V among all the electrolytes we studied, which is even higher than the constant charge voltage of 2.1 V we used in galvanostatic measurements (**Figures 4a-c**). To ensure the MnO_2 deposition in the BF_4-0.9 electrolyte is not limited by the applied voltage, we increased the applied voltage to 2.3 V and retested the device in the BF_4-0.9 electrolyte. Over 160 cycles, the BF_4-0.9 system only shows the maximum CE of 65.23% (**Figure 4e**), which is still substantially lower compared with 99.67% obtained in the BF_4-SO_4-1.5 electrolyte. We believe that the BF_4-H_2O H-bond network in BF_4-0.9 electrolyte severely restricts the supply of water molecules at the electrode/electrolyte interface and, therefore, negatively affects Mn^{2+}/MnO_2 voltage and deposition efficiency. The best deposition efficiency obtained in the hybrid electrolyte BF_4-SO_4-1.5 further demonstrate the significance of balanced proton diffusion (via the BF_4-H_2O H-bond network) and sufficient supply of interfacial water molecules (via non-H-bonded regions) on MnO_2 deposition.
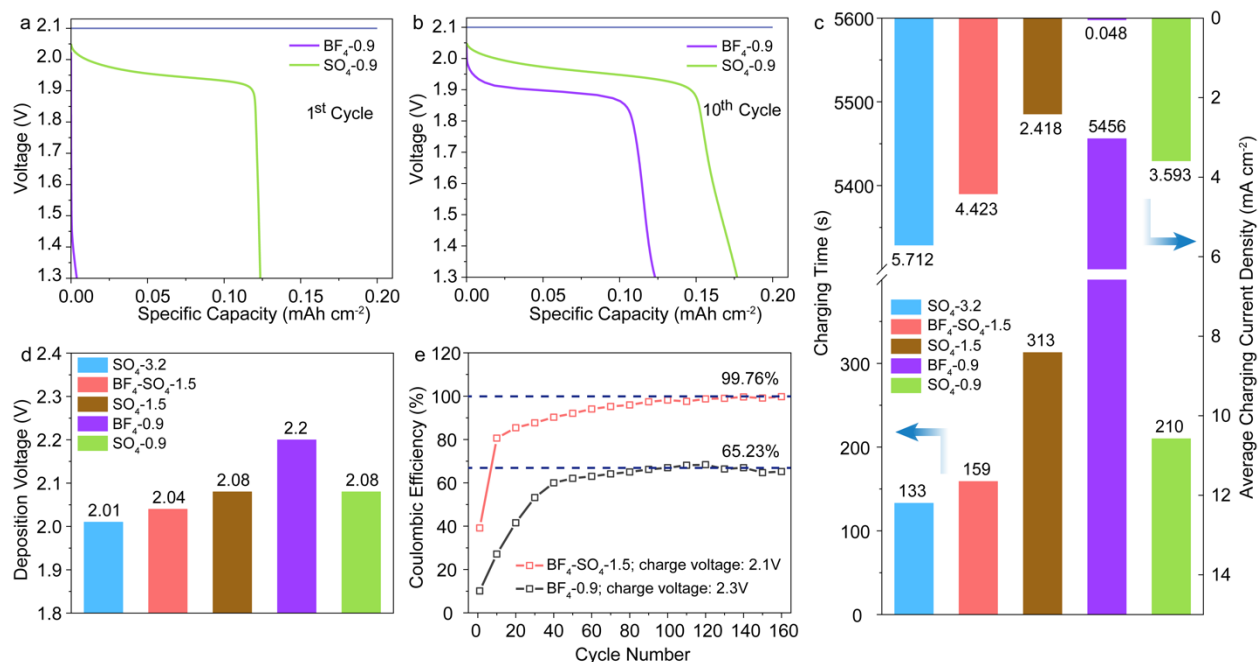
Figure 4. (a) The 1st and (b) 10th galvanostatic discharge curves obtained at 1.0 mA cm^{-2} in different electrolyte systems. (c) The comparison of charging time and charging current density in different electrolytes under a constant charging voltage (2.1 V). (d) The MnO_2 deposition voltages in different electrolytes at a constant current density of 1.0 mA cm^{-2}. (e) The change of devices' CE in BF$_4$-0.9 and BF$_4$-SO$_4$-1.5 electrolyte systems within 160 cycles.

We noticed that a balanced proton and water activity at the interface would also improve the deposition uniformity of MnO_2. **Figures 5a-c** show the morphologies of deposited MnO_2 obtained in three different electrolytes after 200 charge/discharge cycles. First, the MnO_2 was non-uniformly deposited on carbon cloth in SO$_4$-3.2 with lower acidity. While the carbon cloth is fully covered with MnO_2, the deposited film has a high roughness. Compared with SO$_4$-3.2, the deposited MnO_2 film in SO$_4$-1.5 has serious cracking and peeling issue. We believe that is the result of accumulated proton at the interface continuously attacking deposited MnO_2.[21] On the contrary, benefit from the balanced interfacial proton diffusion and water supply, the BF$_4$-SO$_4$-1.5

14

electrolyte enables the uniform and smooth MnO_2 deposition without cracks, even under at a higher capacity (**Figure S9**, Supporting Information). This is critical for large-scale applications.

Besides, BF_4-SO_4-1.5 also shows better compatibility with the zinc metal anode with a uniform surface. **Figure S10** (Supporting Information) shows the zinc stripping/plating efficiency of Zn//Zn symmetric cells in different electrolytes. While the cells achieved 100 % CE over 200 hours in all three electrolytes, the most uniform and smooth zinc anode surface was obtained in BF_4-SO_4-1.5 (**Figures 5d-f**). After stripping/plating in SO_4-1.5 and SO_4-3.2 electrolytes, the anode surfaces were covered with nanosheets. X-ray energy dispersive spectroscopy mapping data confirmed the nanosheets contain S and O signals (**Figure S11a**, Supporting Information), suggesting the formation of zinc hydroxide sulfate (ZHS). This is consistent with the previous reports on the formation of ZHS on zinc anode surface because of disturbed pH.[30-32] Significantly, the anode surface is uniform and free of nanosheets if stripping/plating was performed in BF_4-SO_4-1.5 electrolyte. The Raman spectrum collected from the anode cycled in BF_4-SO_4-1.5 electrolyte suggests the presence of a ZnF_2 containing solid-electrolyte-interface (SEI) layer (**Figure S11b**, Supporting Information). This SEI layer suppresses the formation of other side products and ensures a uniform coating of zinc on the anode surface.[33] Furthermore, we also investigated the zinc stripping/plating efficiency in Zn//Cu asymmetric cells (**Figure S12**, Supporting Information). The hybrid system (BF_4-SO_4-1.5) still has the most stable efficiency of ~99.0% compared with the sulfate electrolytes. In addition, after 100 cycles of testing in Zn//Cu asymmetric cells, the electrode in BF_4-SO_4-1.5 shows a uniform morphology with fine particles rather than large sheets obtained in the sulfate systems (**Figures S12c-e**, Supporting Information). These results reveal the critical role of the hybrid electrolyte in suppressing the ZHS formation and ensuring uniform zinc deposition.
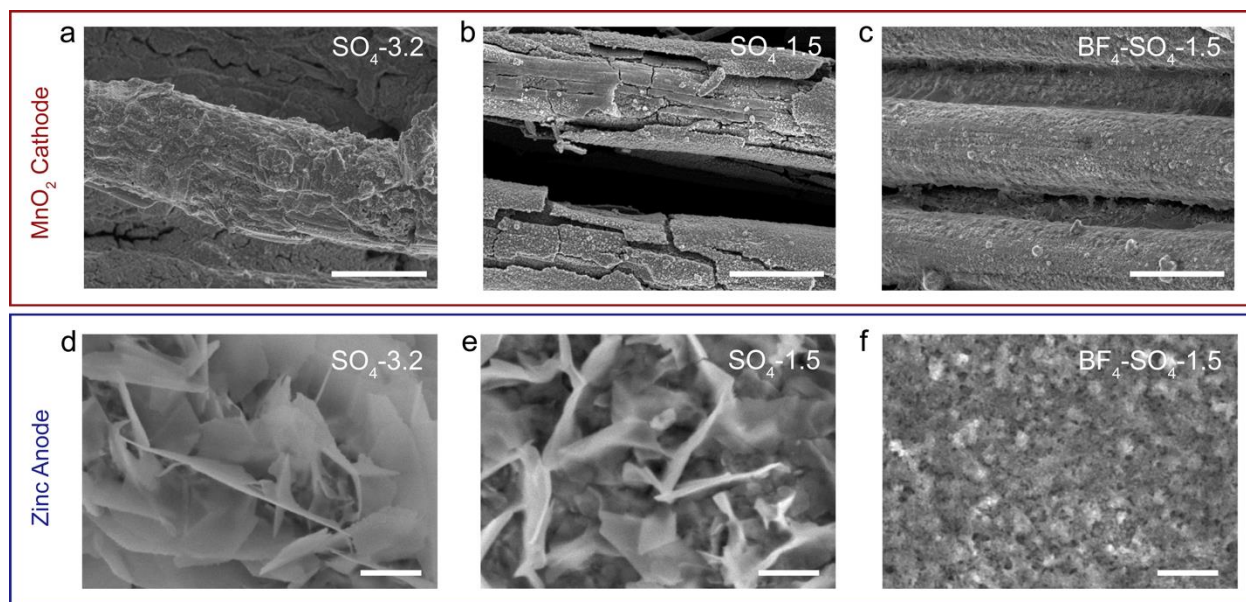
Figure 5. The morphologies of deposited MnO_2 on the carbon cloth cathode of a $Zn//MnO_2$ device after 200 charge/discharge cycles in (a) SO_4-3.2, (b) SO_4-1.5, and (c) BF_4-SO_4-1.5 electrolytes. Scale bars are 10 μm. The zinc surface morphologies of a $Zn//Zn$ symmetric cell after 200 hours' stripping/plating cycles in (d) SO_4-3.2, (e) SO_4-1.5, and (f) BF_4-SO_4-1.5 electrolytes. Scale bars are 500 nm.

A cathode-free $Zn//MnO_2$ electrolytic cell was fabricated and tested in a beaker cell containing 5.0 ml of BF_4-SO_4-1.5 electrolyte (**Figure 6a**). The battery shows an excellent rate performance and well-maintained high-voltage discharge platforms (**Figure 6b**). It achieves a high platform voltage of ~1.92 V at 1.0 mA cm^{-2} (**Figure S13**, Supporting Information) and an outstanding energy efficiency of 84.23%, which are higher than all the reported values for acid-free Zn-MnO_2 battery systems, and even comparable to the acid added systems (**Figure 6c**). Furthermore, the battery's capacity can be further increased to 3.0 mAh cm^{-2} while retaining a good CE of over 90% (**Figure 6d**) and reaching an impressive energy density of 4.76 mWh cm^{-2}

16

(**Table S3**, Supporting Information), revealing its great potential for practical applications. Besides, long-term cycling stability, especially at relatively low rates (0.5 ~ 2 C) is essential for batteries. The cycle life at low rates can be a few times and even an order of magnitude shorter than that at higher rates (5 ~ 30 C) due to the materials and cell degradation.[1] We tested a Zn-MnO$_2$ battery with a capacity of 1.0 mAh cm^{-2} in the hybrid electrolyte (BF$_4$-SO$_4$-1.5) at 1 C, a considerably lower rate compared with previous studies (**Table S3**, Supporting Information). As shown in **Figure 6e**, the battery exhibits the excellent cyclability (~100 CE%) for 1000 cycles. Most importantly, it achieves an outstanding energy efficiency retention rate of 93.65%, indicating the Mn^{2+}/MnO$_2$ conversion is very efficient with a performance degradation per cycle of only ~0.006%. We believe that this superior cyclability at the low rate is because of the efficient Mn^{2+}/MnO$_2$ chemistry via improved interfacial environment. The results again demonstrate the importance of regulating interfacial proton and water activity.
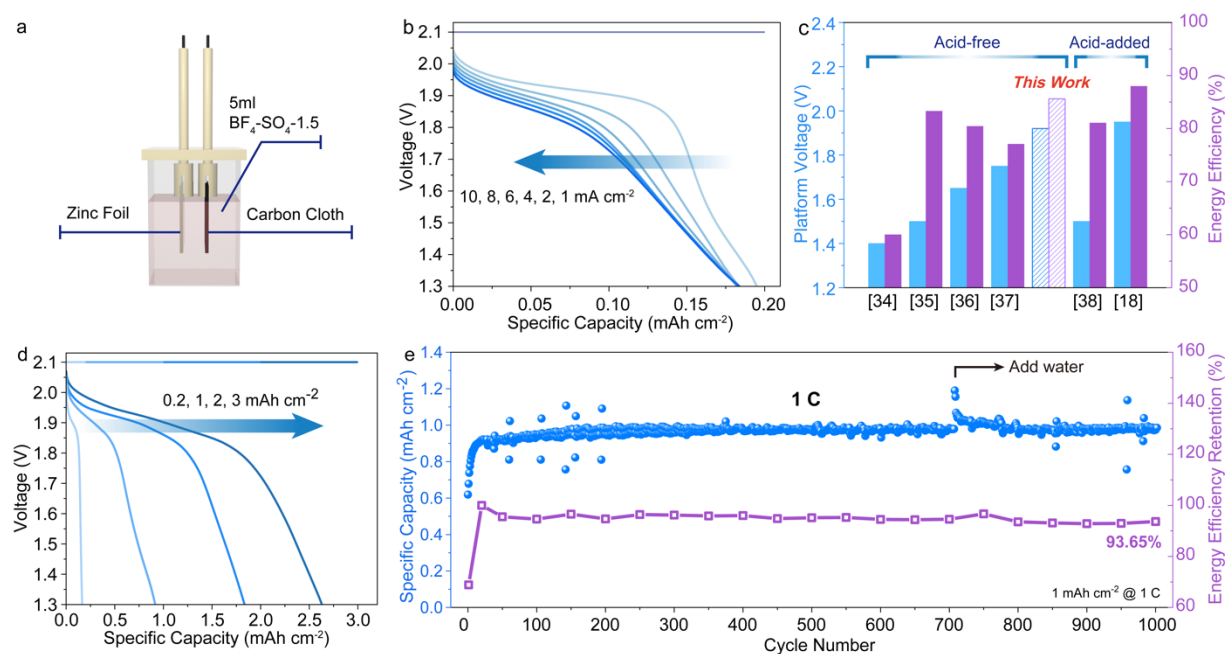

17

Figure 6. (a) Schematic illustration of a cathode-free $Zn//MnO_2$ electrolytic cell tested in a beaker cell configuration. (b) Galvanostatic discharge curves of the device at different current densities, with a constant charge voltage of 2.1 V. (c) A histogram compares the platform voltage and energy efficiency of our device and previously reported devices tested in different electrolytes (from left to right): 3.0 M $ZnCl_2$ + 0.10 M $MnCl_2$,[34] 1.0 M $ZnAc_2$ + 0.4 M $MnAc_2$,[35] 0.25 M $Al_2(SO_4)_3$ + 2 M $ZnSO_4$ + 0.50 M $MnSO_4$,[36] 2 M $ZnCl_2$ + 0.07 M $Mn(H_2PO_4)_2$,[37] 0.50 M $ZnCl_2$ + 0.5 M $MnAc_2$ + 2.0 M KCl + 1.75 M HAc + 0.05 M $CrCl_3$,[38] and 1.0 M $ZnSO_4$ + 1.0 M $MnSO_4$ + 0.10 M H_2SO_4.[18] (d) Galvanostatic discharge curves of devices with different capacities at 1.0 mA cm^{-2}. (e) The capacity and energy efficiency retention of the 1.0 mAh cm^{-2} device over 1000 cycles at 1 C.

In summary, we have demonstrated a new strategy to enhance the Mn^{2+}/MnO_2 platform voltage, conversion efficiency, coating uniformity, and low rate (1 C) cycling stability of aqueous $Zn//MnO_2$ electrolytic batteries by balancing interfacial proton and water activities. The hybrid BF_4-SO_4-1.5 electrolyte not only provides a low pH environment that is preferable for MnO_2 dissolution, but also regulates the proton diffusion and the supply of water molecules for MnO_2 deposition. This study demonstrates the significance of electrolyte design for promoting Mn^{2+}/MnO_2 kinetics and the practicality of MnO_2 electrolytic batteries. This strategy can also potentially be used to improve the performance of other aqueous and non-aqueous MnO_2-based electrochemical energy storage systems such as lithium batteries, proton batteries and supercapacitors.

Supporting Information

The Supporting Information is available free of charge at ...

Experimental and simulation details, materials characterization and electrochemical measurements, table for comparison among different Zn-MnO$_2$ batteries, etc.

Acknowledgements

References

1. Li, C.; Jin, S.; Archer, L. A.; Nazar, L. F., Toward practical aqueous zinc-ion batteries for electrochemical energy storage. *Joule* **2022,** *6* (8), 1733-1738.

2. Song, J.; Xu, K.; Liu, N.; Reed, D.; Li, X., Crossroads in the renaissance of rechargeable aqueous zinc batteries. *Materials Today* **2021,** *45*, 191-212.

3. Zhu, Z.; Jiang, T.; Ali, M.; Meng, Y.; Jin, Y.; Cui, Y.; Chen, W., Rechargeable Batteries for Grid Scale Energy Storage. *Chemical Reviews* **2022,** *122* (22), 16610-16751.

4. Kundu, D.; Adams, B. D.; Duffort, V.; Vajargah, S. H.; Nazar, L. F., A high-capacity and long-life aqueous rechargeable zinc battery using a metal oxide intercalation cathode. *Nature Energy* **2016,** *1* (10), 16119.

5. Pan, H.; Shao, Y.; Yan, P.; Cheng, Y.; Han, K. S.; Nie, Z.; Wang, C.; Yang, J.; Li, X.; Bhattacharya, P.; Mueller, K. T.; Liu, J., Reversible aqueous zinc/manganese oxide energy storage from conversion reactions. *Nature Energy* **2016,** *1* (5), 16039.

6. Li, Y.; Zhao, J.; Hu, Q.; Hao, T.; Cao, H.; Huang, X.; Liu, Y.; Zhang, Y.; Lin, D.; Tang, Y.; Cai, Y., Prussian blue analogs cathodes for aqueous zinc ion batteries. *Materials Today Energy* **2022,** *29*, 101095.

7. Li, Y.; Dai, H., Recent advances in zinc–air batteries. *Chemical Society Reviews* **2014,** *43* (15), 5257-5275.

8. Liu, D.; He, B.; Zhong, Y.; Chen, J.; Yuan, L.; Li, Z.; Huang, Y., A durable ZnS cathode for aqueous Zn-S batteries. *Nano Energy* **2022,** *101*, 107474.

9. Yang, M.; Yan, Z.; Xiao, J.; Xin, W.; Zhang, L.; Peng, H.; Geng, Y.; Li, J.; Wang, Y.; Liu, L.; Zhu, Z., Boosting Cathode Activity and Anode Stability of Zn-S Batteries in Aqueous

Media Through Cosolvent-Catalyst Synergy. *Angewandte Chemie International Edition* **2022,** *61* (42), e202212666.

10.   Zhang, S.-J.; Hao, J.; Li, H.; Zhang, P.-F.; Yin, Z.-W.; Li, Y.-Y.; Zhang, B.; Lin, Z.; Qiao, S.-Z., Polyiodide Confinement by Starch Enables Shuttle-Free Zn–Iodine Batteries. *Advanced Materials* **2022,** *34* (23), 2201716.

11.   Lin, D.; Rao, D.; Chiovoloni, S.; Wang, S.; Lu, J. Q.; Li, Y., Prototypical Study of Double-Layered Cathodes for Aqueous Rechargeable Static Zn–I2 Batteries. *Nano Letters* **2021,** *21* (9), 4129-4135.

12.   Sambandam, B.; Mathew, V.; Kim, S.; Lee, S.; Kim, S.; Hwang, J. Y.; Fan, H. J.; Kim, J., An analysis of the electrochemical mechanism of manganese oxides in aqueous zinc batteries. *Chem* **2022,** *8* (4), 924-946.

13.   Zhong, C.; Liu, B.; Ding, J.; Liu, X.; Zhong, Y.; Li, Y.; Sun, C.; Han, X.; Deng, Y.; Zhao, N.; Hu, W., Decoupling electrolytes towards stable and high-energy rechargeable aqueous zinc–manganese dioxide batteries. *Nature Energy* **2020,** *5* (6), 440-449.

14.   Liu, Z.; Qin, L.; Lu, B.; Wu, X.; Liang, S.; Zhou, J., Issues and Opportunities Facing Aqueous Mn2+/MnO2-based Batteries. *ChemSusChem* **2022,** *15* (10), e202200348.

15.   Chen, W.; Li, G.; Pei, A.; Li, Y.; Liao, L.; Wang, H.; Wan, J.; Liang, Z.; Chen, G.; Zhang, H.; Wang, J.; Cui, Y., A manganese–hydrogen battery with potential for grid-scale energy storage. *Nature Energy* **2018,** *3* (5), 428-435.

16.   Wang, M.; Zheng, X.; Zhang, X.; Chao, D.; Qiao, S.-Z.; Alshareef, H. N.; Cui, Y.; Chen, W., Opportunities of Aqueous Manganese-Based Batteries with Deposition and Stripping Chemistry. *Advanced Energy Materials* **2021,** *11* (5), 2002904.

17.   Chao, D.; Zhou, W.; Xie, F.; Ye, C.; Li, H.; Jaroniec, M.; Qiao, S.-Z., Roadmap for advanced aqueous batteries: From design of materials to applications. *Science Advances* **2020,** *6* (21), eaba4098.

18.   Chao, D.; Zhou, W.; Ye, C.; Zhang, Q.; Chen, Y.; Gu, L.; Davey, K.; Qiao, S.-Z., An Electrolytic Zn–MnO2 Battery for High-Voltage and Scalable Energy Storage. *Angewandte Chemie International Edition* **2019,** *58* (23), 7823-7828.

19.   Liu, Z.; Li, L.; Qin, L.; Guo, S.; Fang, G.; Luo, Z.; Liang, S., Balanced Interfacial Ion Concentration and Migration Steric Hindrance Promoting High-Efficiency Deposition/Dissolution Battery Chemistry. *Advanced Materials* **2022,** *34* (40), 2204681.

20.   Yang, H.; Chen, D.; Zhao, R.; Li, G.; Xu, H.; Li, L.; Liu, X.; Li, G.; Chao, D.; Han, W., Reunderstanding aqueous Zn electrochemistry from interfacial specific adsorption of solvation structures. *Energy & Environmental Science* **2023**.

21.   Ye, X.; Han, D.; Jiang, G.; Cui, C.; Guo, Y.; Wang, Y.; Zhang, Z.; Weng, Z.; Yang, Q.-H., Unraveling the deposition/dissolution chemistry of MnO2 for high-energy aqueous batteries. *Energy & Environmental Science* **2023,** *16* (3), 1016-1023.

22.   Saihara, K.; Yoshimura, Y.; Fujimoto, H.; Shimizu, A., Detrimental effect of glass sample tubes on investigations of BF4−-based room temperature ionic liquid–water mixtures. *Journal of Molecular Liquids* **2016,** *219*, 493-496.

23.   Wamser, C. A., Hydrolysis of fluoboric acid in aqueous solution. *Journal of the American Chemical Society* **1948,** *70* (3), 1209-1215.

24.   Sun, T.; Yuan, X.; Wang, K.; Zheng, S.; Shi, J.; Zhang, Q.; Cai, W.; Liang, J.; Tao, Z., An ultralow-temperature aqueous zinc-ion battery. *Journal of Materials Chemistry A* **2021,** *9* (11), 7042-7047.

25.   Shi, Y.; Wang, R.; Bi, S.; Yang, M.; Liu, L.; Niu, Z., An Anti-Freezing Hydrogel Electrolyte for Flexible Zinc-Ion Batteries Operating at −70 °C. *Advanced Functional Materials* **2023,** *33* (33), 2214546.

26.   Ma, Z.; Shi, X.-M.; Nishimura, S.-i.; Ko, S.; Okubo, M.; Yamada, A., Anhydrous Fast Proton Transport Boosted by the Hydrogen Bond Network in a Dense Oxide-Ion Array of α-MoO3. *Advanced Materials* **2022,** *34* (34), 2203335.

27.   Su, Z.; Chen, J.; Stansby, J.; Jia, C.; Zhao, T.; Tang, J.; Fang, Y.; Rawal, A.; Ho, J.; Zhao, C., Hydrogen-Bond Disrupting Electrolytes for Fast and Stable Proton Batteries. *Small* **2022,** *18* (22), 2201449.

28.   Chuai, M.; Yang, J.; Tan, R.; Liu, Z.; Yuan, Y.; Xu, Y.; Sun, J.; Wang, M.; Zheng, X.; Chen, N.; Chen, W., Theory-Driven Design of a Cationic Accelerator for High-Performance Electrolytic MnO2–Zn Batteries. *Advanced Materials* **2022,** *34* (33), 2203249.

29.   Chao, D.; Ye, C.; Xie, F.; Zhou, W.; Zhang, Q.; Gu, Q.; Davey, K.; Gu, L.; Qiao, S.-Z., Atomic Engineering Catalyzed MnO2 Electrolysis Kinetics for a Hybrid Aqueous Battery with High Power and Energy Density. *Advanced Materials* **2020,** *32* (25), 2001894.

30.   Li, Q.; Han, L.; Luo, Q.; Liu, X.; Yi, J., Towards Understanding the Corrosion Behavior of Zinc-Metal Anode in Aqueous Systems: From Fundamentals to Strategies. *Batteries & Supercaps* **2022,** *5* (4), e202100417.

31.   Du, W.; Ang, E. H.; Yang, Y.; Zhang, Y.; Ye, M.; Li, C. C., Challenges in the material and structural design of zinc anode towards high-performance aqueous zinc-ion batteries. *Energy & Environmental Science* **2020,** *13* (10), 3330-3360.

32.	Yu, X.; Li, Z.; Wu, X.; Zhang, H.; Zhao, Q.; Liang, H.; Wang, H.; Chao, D.; Wang, F.; Qiao, Y.; Zhou, H.; Sun, S.-G., Ten concerns of Zn metal anode for rechargeable aqueous zinc batteries. *Joule* **2023**.

33.	Han, D.; Cui, C.; Zhang, K.; Wang, Z.; Gao, J.; Guo, Y.; Zhang, Z.; Wu, S.; Yin, L.; Weng, Z.; Kang, F.; Yang, Q.-H., A non-flammable hydrous organic electrolyte for sustainable zinc batteries. *Nature Sustainability* **2022,** *5* (3), 205-213.

34.	Lv, H.; Song, Y.; Qin, Z.; Zhang, M.; Yang, D.; Pan, Q.; Wang, Z.; Mu, X.; Meng, J.; Sun, X.; Liu, X.-X., Disproportionation enabling reversible MnO2/Mn2+ transformation in a mild aqueous Zn-MnO2 hybrid battery. *Chemical Engineering Journal* **2022,** *430*, 133064.

35.	Zeng, X.; Liu, J.; Mao, J.; Hao, J.; Wang, Z.; Zhou, S.; Ling, C. D.; Guo, Z., Toward a Reversible Mn4+/Mn2+ Redox Reaction and Dendrite-Free Zn Anode in Near-Neutral Aqueous Zn/MnO2 Batteries via Salt Anion Chemistry. *Advanced Energy Materials* **2020,** *10* (32), 1904163.

36.	Qin, Z.; Song, Y.; Yang, D.; Zhang, M.-Y.; Shi, H.-Y.; Li, C.; Sun, X.; Liu, X.-X., Enabling Reversible MnO2/Mn2+ Transformation by Al3+ Addition for Aqueous Zn–MnO2 Hybrid Batteries. *ACS Applied Materials & Interfaces* **2022,** *14* (8), 10526-10534.

37.	Liu, Y.; Qin, Z.; Yang, X.; Liu, J.; Liu, X.-X.; Sun, X., High-Voltage Manganese Oxide Cathode with Two-Electron Transfer Enabled by a Phosphate Proton Reservoir for Aqueous Zinc Batteries. *ACS Energy Letters* **2022,** *7* (5), 1814-1819.

38.	Liu, Z.; Yang, Y.; Lu, B.; Liang, S.; Fan, H. J.; Zhou, J., Insights into complexing effects in acetate-based Zn-MnO2 batteries and performance enhancement by all-round strategies. *Energy Storage Materials* **2022,** *52*, 104-110.

Table of Contents Entry
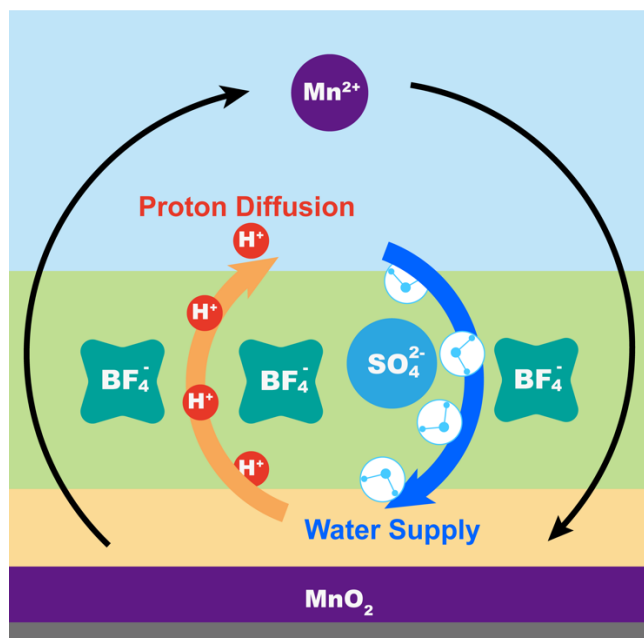
A hybrid electrolyte regulates interfacial proton diffusion and water supply to facilitate Mn^{2+}/MnO_2 two-electron transfer in MnO_2 electrolytic batteries.